

# Dynamic Precipitation in Supersaturated Al–Zn–Mg–Cu Alloy During Warm Stretching



JOSEPH ROBSON, PETER JESSNER, MARK TAYLOR, and ZIYU MA

High-strength Al–Zn–Mg–Cu alloys such as AA7075 rely on precipitation to obtain their properties, and the evolution of these precipitates can be strongly influenced by deformation. In this study, the effect of warm stretching on precipitation in supersaturated AA7075 was investigated. A dilatometer was used to enable rapid quenching directly from the solution treatment temperature to the warm stretching temperature. The evolution of precipitates was monitored using small-angle X-ray scattering (SAXS) and transmission electron microscopy (TEM). SAXS revealed the presence of clusters only 5 seconds after quenching, and the subsequent evolution of the microstructure involved the growth and coarsening of these clusters. Deformation strongly enhanced the cluster/precipitate growth rate, which increased linearly with increasing strain. A strain rate effect was also noted, with the growth rate being faster at the higher strain rate for the same strain level. However, the acceleration of growth with increasing strain rate was not sufficient to compensate for the reduced time, so that deformation at higher strain rate led to small precipitates (at iso-strain). TEM revealed the precipitates to be homogeneously dispersed in the matrix both with and without deformation. There was no evidence for enhanced nucleation due to deformation, indeed the opposite was the case, with fewer but larger precipitates observed in the deformed microstructure. The linear increase in growth rate with strain is consistent with a dominant effect of excess vacancies in enhancing diffusion rates.

<https://doi.org/10.1007/s11661-023-06962-9>

© The Authors 2023

## I. INTRODUCTION

**STRONG** aluminum alloys obtain their properties through the formation of a controlled distribution of nano-scale precipitates. It is now well established that deformation can profoundly influence the evolution of these precipitates.<sup>[1–4]</sup> The coupled effect of deformation and temperature on the precipitates in aluminum alloys is particularly important in warm forming, creep age forming, high-pressure torsion, and fatigue, where strong dynamic interactions can occur.<sup>[1–3,5–7]</sup>

It has previously been demonstrated that the growth of a pre-existing precipitate population can be greatly enhanced by warm deformation.<sup>[2,4]</sup> In these studies, a dominant role for strain-induced excess vacancies was identified in enhancing diffusivity.<sup>[2,3,6,8]</sup> Excess

vacancies are produced by the non-conservative movement of jogs on dislocations, consuming a small portion of the applied mechanical work.<sup>[9,10]</sup> The excess vacancies influence diffusivity and other kinetic processes governing precipitation.<sup>[3]</sup> Further details of the excess vacancy effect are given elsewhere.<sup>[11]</sup>

One important factor in determining which dynamic effects will be observed is the initial microstructural state of the material and in particular the level of supersaturation at the deformation temperature. Most previous studies have focused on material deformed in a pre-tempered condition where there is an existing distribution of precipitates.<sup>[2]</sup> Even in cases where the initial starting condition of the material was solution treated and quenched, the natural aging that occurs in aluminum alloys plus the rapid initial precipitate evolution during heating means that significant changes will occur before deformation is applied.<sup>[4]</sup> In such cases, it has been demonstrated that the main effect of deformation is to accelerate the growth and coarsening of the existing precipitates rather than nucleate new particles. On the other hand, at room temperature, it has been shown that cyclic deformation of an initially supersaturated matrix leads to accelerated decomposition through the nucleation of new GP zones.<sup>[3,6]</sup> The significance of deformation on nucleation *vs* accelerated growth of

JOSEPH ROBSON, MARK TAYLOR, and ZIYU MA are with the Department of Materials, University of Manchester, Oxford Road, Manchester, M13 9PL, UK. Contact e-mails: joseph.d.robson@manchester.ac.uk; ziyu.ma@manchester.ac.uk  
PETER JESSNER is with the Constellium Technology Center, CS 10027, 38341, Voreppe, France.

Manuscript submitted July 27, 2022; accepted January 9, 2023.

Article published online February 10, 2023

precipitates is not yet established for the industrially important case of warm deformation, where the initial condition is strongly supersaturated.

A key aim of the present study was to investigate the effect of warm deformation on precipitate evolution in a case where the initial matrix is as supersaturated as possible. In an industrial context, this would be most relevant in a case where forming occurs directly after solution treatment. To achieve this, the final solution treatment and warm deformation must be performed in a combined process so that precipitation does not occur between steps by natural aging or during pre-heat.

## II. METHODOLOGY

The material used in this study was 7075 aluminum alloy sheet of 1.5 mm thickness produced from commercially direct-chill cast and rolled plate, supplied in the F temper (as fabricated) by Constellium Technology Center (France) with the nominal composition shown in Table I.

Deformation and heating were performed using a TA Instruments DIL 805 A/D/T dilatometer. This instrument allows accurate temperature control (to within 0.1 °C), rapid specimen heating and cooling (up to 100 °C s<sup>-1</sup> when working in the tension mode), and controlled strain rates of up to 1 s<sup>-1</sup>. The sample geometry for testing in the dilatometer is shown in Figure 1.

Prior to loading in the dilatometer solution heat treatment was first performed at 480 °C in an air recirculating furnace for 1.5 h, followed by water quenching to room temperature. This dissolves the large precipitates present in the F-temper condition and reduces the time necessary to achieve a fully solutionized condition in the dilatometer.

To reverse any undesired natural aging during the transport and equipment setup, specimens were subject to a second short solution treatment of 10 minutes in the dilatometer itself at the same temperature of 480 °C (using a heating rate of 10 °C s<sup>-1</sup>). Samples were subsequently gas quenched (using nitrogen) to 180 °C followed by an additional 5 seconds of holding to stabilize the temperature. The aim was to minimize the precipitation that occurs before applying deformation.

Two deformation strain rates were used, with an approximately order of magnitude difference. Average strain rates were calculated by fitting a linear function on the strain–time plot. Nominal average strain rates of 7 × 10<sup>-4</sup> and 6 × 10<sup>-3</sup> s<sup>-1</sup> were measured for slow and fast deformation. The evolution of the specimen elongation was measured using push-rods, which was then converted into the true strain variation, monitored

throughout deformation. Tests were interrupted at different values of plastic strain to study the dynamic precipitation evolution. Upon reaching the target final strain, unloading and gas quenching were performed simultaneously. The unloading was essential to prevent further plastic strain due to thermal contraction, and this was confirmed by monitoring the load on the specimen. Reference samples were also produced in the dilatometer. These underwent exactly the same thermal history, but without any deformation. To ensure no deformation due to thermal expansion or contraction, the dilatometer was operated in load control and the specimen was allowed to freely expand and contract as the temperature changed.

Figure 2 demonstrates an example thermal history for a sample solution heat treated 10 minutes at 480 °C followed by gas quenching to 180 °C for tensile tests with 6 × 10<sup>-3</sup> and 7 × 10<sup>-4</sup> s<sup>-1</sup> strain rate. The average quenching rates after solution heat treatment and deformation were measured as 149 °C and 68 °C s<sup>-1</sup>, respectively. Stable temperature control was obtained with ± 0.9 °C standard deviation from the target temperature throughout the test.

After dilatometer testing, all samples were stored at – 23 °C in a freezer to prevent any further precipitate evolution prior to being prepared for the SAXS measurements.

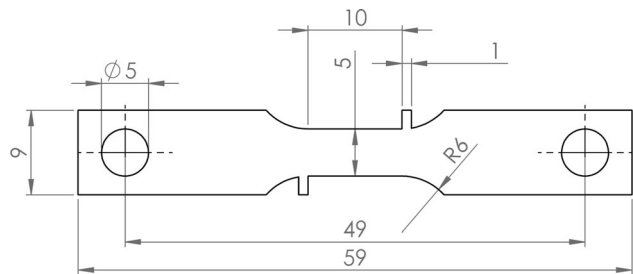


Fig. 1—Test sample geometry used for dilatometer experiments. All dimensions are in mm.

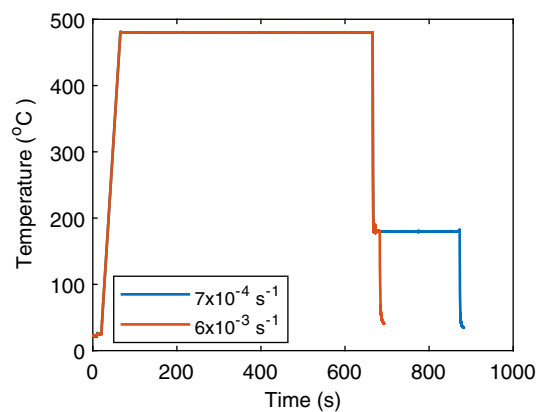


Fig. 2—The temperature profile of sample solution heat treated at 480 °C followed by the deformation at 180 °C. Online version in color.

Table I. Nominal Composition of AA7075 in Wt Pct

	Zn	Mg	Cu	Si	Fe	Mn	Cr	Al
AA7075	5.6	2.5	1.6	0.2	0.25	0.15	0.23	Bal

Immediately before being dispatched for analysis, samples were taken from the freezer. The grip area was removed using a Struers Accutom-5 precision cut-off machine with a feed speed of  $0.05 \text{ mm s}^{-1}$ , giving a total time of 4 minutes to remove both grip sections. The gauge area was mechanically ground to  $70 \mu\text{m}$  thickness for small-angle x-ray scattering (SAXS) characterization. The time at room temperature between removal from the freezer and SAXS measurement was approximately 7 days. SAXS experiments were performed at DL-SAXS Diamond Light Source on a Xeuss 3.0 instrument, which equipped an Excillum Gallium MetalJet x-ray source providing  $9.2 \text{ keV}$  energy and an Eiger2 R 1M silicon detector with a pixel size of 75 microns. The camera length was selected as  $0.5 \text{ m}$  to provide a useful scattering vector range  $[0.009, 0.6] \text{ \AA}^{-1}$ . The 2-dimensional scattering patterns of each sample were collected using a 600 s of exposure time. Since the scattering patterns were isotropic, the average results and standard deviations were calculated by doing a circular average of scattering signals at each scattering vector  $q$ .

Analysis of the SAXS results was performed using procedures described in detail in Reference 12. Briefly, from the SAXS data, the Guinier radius can be calculated using the scattering vector  $q$  corresponded to the peak in the Kratky plot, as shown in Eq. [1].<sup>[1,12]</sup>

$$R_g = \frac{\sqrt{3}}{q_{\text{peak}}} \quad [1]$$

The relation between the Guinier radius  $R_g$  and true radius depends on the shape of the particles. With the hypothesis of spherical geometry at the early stage of precipitation, which is considered reasonable for the precipitates in 7xxx alloys,<sup>[13]</sup> the true radius can be estimated as  $\sqrt{5/3} \cdot R_g$ . Further assuming the precipitate composition is near constant, the volume fraction of precipitates is proportional to the integrated intensity of the Kratky plot. The relative precipitate number density can then be estimated by dividing the integrated intensity (as a proxy for the volume fraction) by the average volume of individual precipitate. In the present study, the morphology of small precipitates is close to spherical, which will be demonstrated in TEM images later. Further considering Guinier radius as a good representation of the average precipitate radius, the average volume of each precipitate is, therefore, proportional to the cube of Guinier radius ( $R_g^3$ ). The number density can then be estimated by dividing the area of the Kratky plot by  $R_g^3$ .

Before producing the Kratky plot, Porod plots ( $Iq^4$  vs  $q^4$ ) were analyzed to identify the background noise caused by the Laue scattering of the disordered solid solution and instrument noise.<sup>[12]</sup> This noise intensity was then subtracted from the total scattering intensity. Further details of the use of SAXS to analyze precipitates in aluminum alloys can be found elsewhere.<sup>[12,14,15]</sup>

To complement SAXS and provide local and spatially resolved information about the precipitates, transmission electron microscopy (TEM) was performed on samples cut from the same ground specimens as for SAXS. Twin jet electropolishing was performed at  $15 \text{ V}$  and  $-40^\circ\text{C}$  in nitric acid and methanol solution (1:3 vol pct) to produce electron transparent areas. Afterward, samples were further thinned by using a Gatan precision ion polishing system (PIPS II) with Ar ions under dual-beam modulation with  $\pm 4^\circ$  gun angles. The polishing sequence was set as 5 minutes at  $1 \text{ keV}$  followed by 10 minutes at  $0.5 \text{ keV}$  and finally 15 minutes at  $0.1 \text{ keV}$ . TEM was performed on a FEI Talos machine equipped with a X-FEG field emission gun operating at an accelerating voltage of  $200 \text{ kV}$ . All images were captured in bright field mode with the diffraction patterns taken along  $\langle 110 \rangle$  zone axis to identify the precipitate phase. On the bright-field images, the precipitates were manually selected and their projected area measured using ImageJ. This was used to calculate the precipitate size as the radius of a circle of equal area. At least 100 precipitates were analyzed in each condition.

### III. RESULTS

The stress–strain responses for specimens in all test conditions are shown in Figure 3(a). Slightly higher ( $< 20 \text{ MPa}$  greater) yield and flow stresses were recorded for specimens deformed at the slower strain rate. Specimens deformed to different levels of strain but under otherwise identical conditions show overlapping curves as expected, demonstrating the high level of repeatability of the experiments. The work hardening rate was calculated from the stress–strain data and is shown in Figure 3(b). This demonstrates that there is no large difference between work hardening rate at the different strain rates.

Figures 4(a) and (b) show example bright-field TEM images of the microstructure of the sample deformed to 12 pct strain with  $7 \times 10^{-4} \text{ s}^{-1}$  strain rate at various magnifications. A fine and homogeneous distribution of nano-scale precipitates can be seen, which are identified as  $\eta'$  from the diffraction pattern (inset). In the low-magnification image (Figure 4(a)) some much larger particles are also observed (10 to 100 nm in length) which are consistent with the size and morphology expected for the E-phase (Cr rich) dispersoids.<sup>[16]</sup>

As a comparison for the deformed case, the microstructure of the non-deformed (but otherwise identically heat treated) material is shown in Figures 4(c) and (d). A similar microstructure and spatial distribution of precipitates is observed as in the deformed sample (Figures 4(a) and (b)). In the deformed sample, the precipitates are slightly larger and more widely spaced than in the non-deformed condition (compare (b) and (d)). From the TEM images, the morphology of small precipitates is close to spherical. The average radius is  $0.8 \pm 0.2 \text{ nm}$  for the deformed

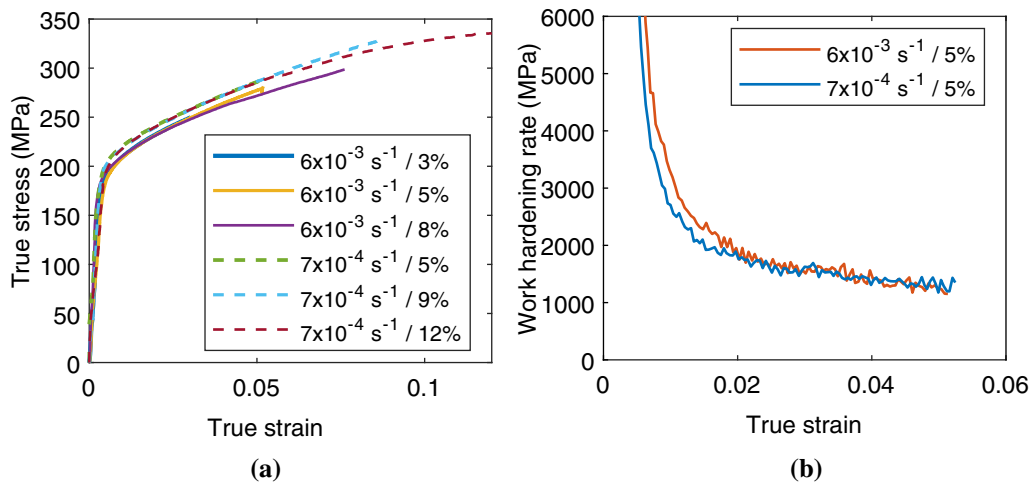


Fig. 3—(a) true stress–strain curves of samples deformed at 180°C with different strains and strain rates. (b) work hardening rate calculated from samples deformed with  $6 \times 10^{-3}$  and  $7 \times 10^{-4} \text{ s}^{-1}$  strain rate to 5 pct strain. Online version in color.

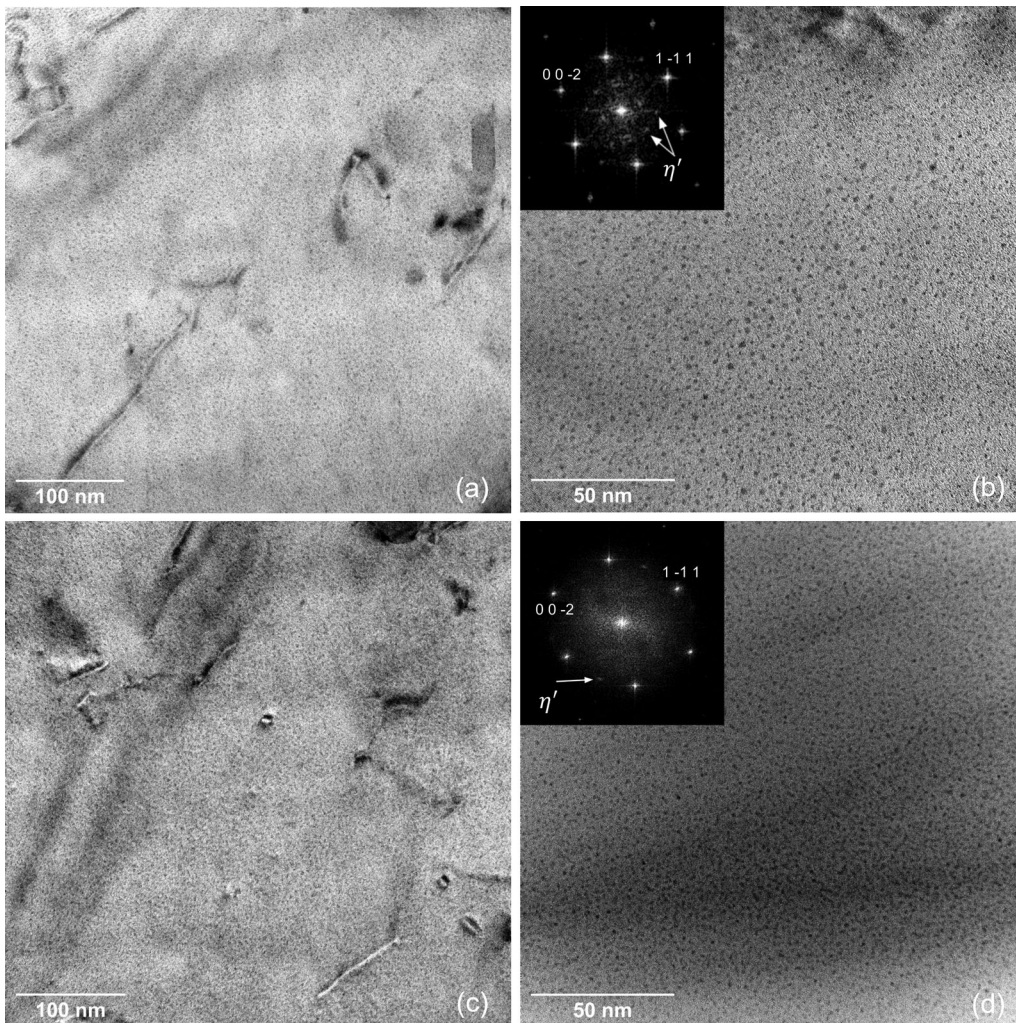


Fig. 4—Bright-field TEM images taken along  $\langle 110 \rangle$  zone axis. (a) and (b) from the sample deformed at 180°C with  $7 \times 10^{-4} \text{ s}^{-1}$  strain rate to 12 pct strain. (c) and (d) from the sample having identical heat treatments as (a) and (b) but without deformation.

case, which is larger than  $0.5 \pm 0.2$  nm for the non-deformed sample.

To obtain a quantitative comparison of the precipitate parameters as a function of strain and strain rate, SAXS was used. This enables a larger and more statistically significant volume of material to be investigated in a more efficient way than is possible with the TEM. The results from the SAXS experiments are shown as Kratky plots in Figure 5.

The  $x$ -axis of these plots shows the scattering vector ( $q$ ), which is inversely proportional to the precipitate size. A shift of the peak toward the left therefore represents a growth in the modal average size. The area under each curve scales with the volume fraction, under the assumption that the precipitate composition is approximately invariant. Figures 5(a) and (b) show the evolution of the Kratky plot with increased strain (which also means increasing time) for (a) the lower and (b) the higher strain rate. As expected, increasing strain and time leads to a shift in the curves to the left and upwards, representing both an increase in the

average precipitate size and volume fraction. The change is most pronounced at the lower strain rate, noting that the time to reach each strain level is approximately 10 times longer in this case. The changes over the much shorter duration of the higher strain rate deformation are smaller, but still significant.

Figure 5(c) compares the plots from the higher and lower strain rate for the case of a high level of strain (8 to 9 pct) and similar strain levels (near iso-strain). The lower strain rate and longer time condition has led to more precipitate growth and a greater volume fraction. Figure 5(d) compares the shortest time at the lower strain rate with the longest time at the higher strain rate. Although the time at the higher strain rate is slightly less than half that at the slower strain rate, the Kratky plots for both conditions are very similar. Indeed, the faster strain rate but shorter time has led to a slightly larger area under the curve and a shift in the peak toward slightly larger particle sizes. This indicates that the higher strain rate is able to partly compensate for the

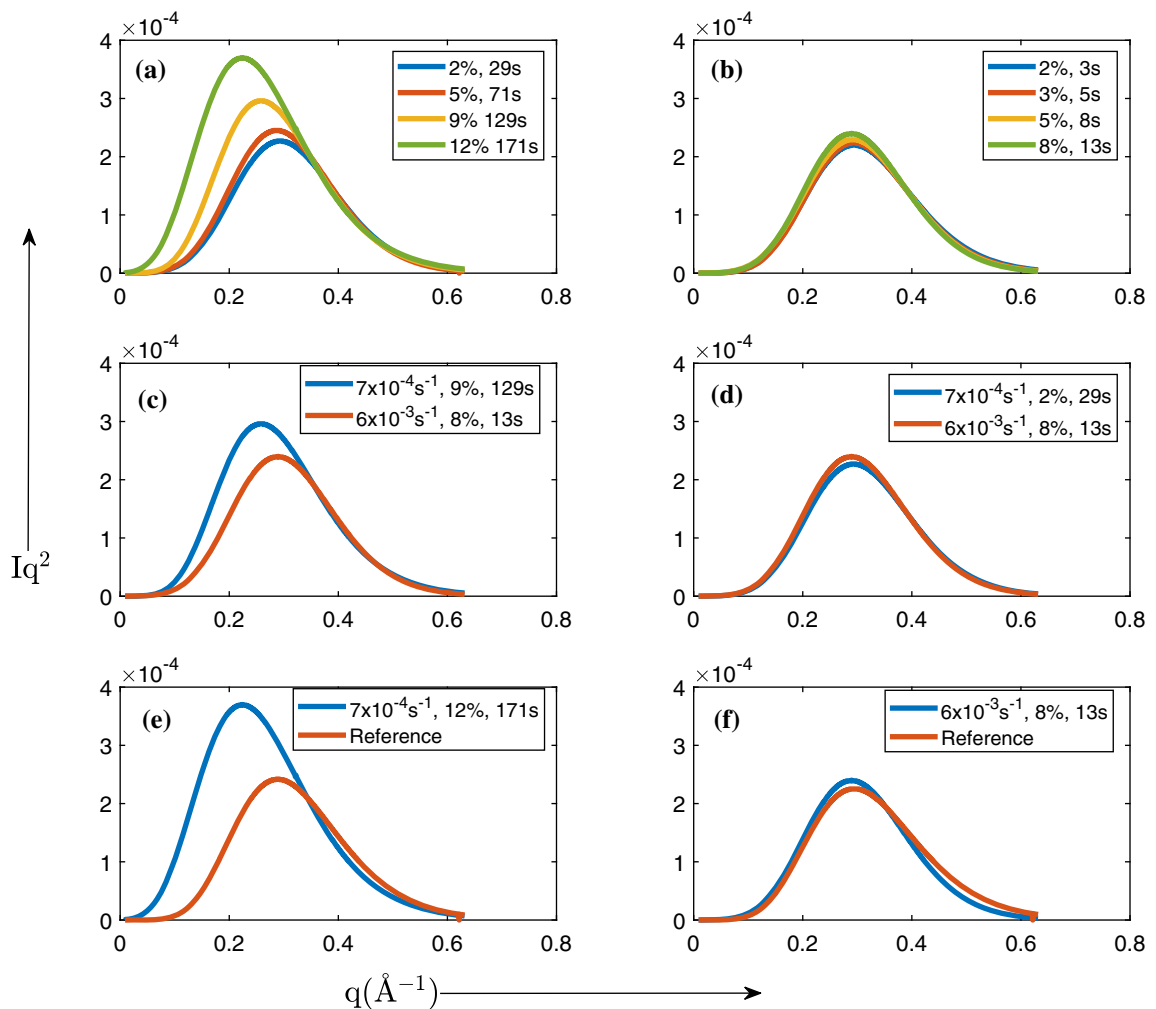


Fig. 5—Kratky plots of SAXS results. (a) samples deformed with  $7 \times 10^{-4} \text{ s}^{-1}$  strain rate. (b) samples deformed with  $6 \times 10^{-3} \text{ s}^{-1}$  strain rate. (c) samples deformed to approximately 9 pct strain. (d) sample deformed at  $6 \times 10^{-3} \text{ s}^{-1}$  for 13s (longest time) and  $7 \times 10^{-4} \text{ s}^{-1}$  for 29s (shortest time) (e) sample deformed to 12 pct strain at  $7 \times 10^{-4} \text{ s}^{-1}$  strain rate, compared to equivalent non-deformed material. (f) sample deformed to 8 pct strain at  $6 \times 10^{-3} \text{ s}^{-1}$  strain rate, compared to equivalent non-deformed condition. Online version in color.

reduction in time, as will be explored in more detail later.

Figures 5(e) and (f) compare the Kratky plots at the highest strain (for lower and higher strain rates, respectively) with those for the reference (non-deformed) condition heated for the same times. At the slower strain rate and hence longer time, it can be seen that the deformation has had a strong effect in shifting the peak upwards and toward larger particle size. At the faster strain rate, and hence shorter time, the same trend is observed but is less pronounced.

These plots demonstrate that deformation plays a significant role in controlling the precipitate evolution, but to understand this better it is necessary to decouple the effects of strain, strain rate, and time (since a lower strain rate necessarily means a longer holding time at iso-strain).

Figure 6 shows the effect of increasing time and strain on the evolution of the Guinier radius and the growth rate (defined as the rate of change of Guinier radius with time). Firstly, the precipitate size determined from SAXS using Eq. [1] is summarized in Table II, which can be compared to the precipitate size determined from TEM. After deforming at a slow strain rate ( $7 \times 10^{-4}$

$s^{-1}$ ) to 12 pct strain, the measured Guinier radius of the precipitates was  $0.77 \pm 0.06$  nm, which is equivalent to a true radius of  $1.0 \pm 0.1$  nm. This is in close agreement with the average radius measured from TEM images ( $0.8 \pm 0.2$  nm). Some discrepancy is expected due to the difference in how precipitates are detected in SAXS and TEM.<sup>[15]</sup>

The effect of deformation on the evolution of average precipitate size can now be considered. Figure 6(a) shows clearly an effect of deformation on the change of Guinier radius with time. In both higher and lower strain rate cases, the difference between the deformed and non-deformed case becomes greater as the time (and hence strain) increases. By plotting the Guinier radius as a function of strain (Figure 6(b)) it can be seen that at low strains (< 5 pct) both higher and lower strain rates show a similar trend, but at high strains (> 5 pct) the Guinier radius for a slower strain rate exceeds that at a higher strain rate (at iso-strain).

Plotting the growth rate (Figures 6(c) and (d)) more clearly highlights the differences between the cases. For the non-deformed condition, the growth rate is very low across the whole time period and falls slightly with increasing time. For both higher and lower strain rate

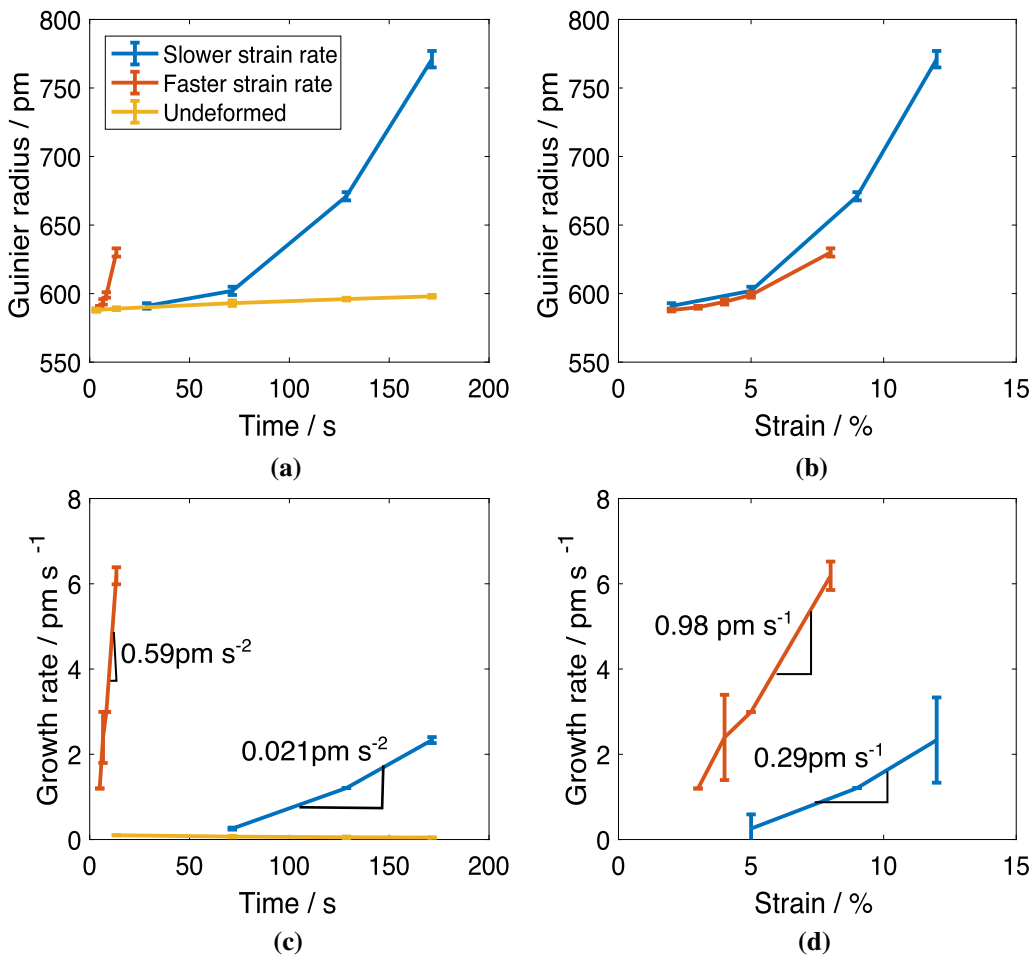


Fig. 6—(a) Evolution of Guinier radius for the slower ( $7 \times 10^{-4} s^{-1}$ ) and faster ( $6 \times 10^{-3} s^{-1}$ ) strain rates compared with the non-deformed case with (a) time, (b) strain. Calculated growth rate for faster and slower strain rates compared with the non-deformed case plotted as a function of (c) time, (d) strain. Online version in color.

**Table II. Guinier Radius of Deformed Samples Determined from SAXS**

Strain Rate (s <sup>-1</sup> )	Strain (Pct)	Guinier Radius (pm)
6 × 10 <sup>-3</sup>	2	589 ± 1
	3	590 ± 1
	4	594 ± 2
	5	599 ± 2
	8	630 ± 3
7 × 10 <sup>-4</sup>	2	591 ± 2
	5	602 ± 3
	9	671 ± 3
	12	771 ± 6

deformed cases, the growth rate increases with time and strain. The change in growth rate with time is approximately linear. The gradient of these lines gives growth acceleration, which can be seen to be approximately 30 times higher in the case of the higher strain rate compared with the lower strain rate. Although this difference is large, it is not sufficient to compensate for the reduction in time at higher strain rate. For example, for the Guinier radius to reach the same value at higher strain rate compared to lower strain rate (at iso-strain) the acceleration of the growth rate at the higher strain rate would have to be 73 times that at the slower strain rate ( $\frac{\dot{\epsilon}_{fast}^2}{\dot{\epsilon}_{slow}^2}$ ). This is because the amount of growth is related to the acceleration of growth rate multiplied by the square of the time.

The change in growth rate with strain can also be plotted as a function of strain (Figure 6(d)). This demonstrates that the higher strain rate does lead to a greater increase in the growth rate for a given level of strain, and the increase is approximately linear (within error). The increase in growth rate with strain (the best-fit gradient of these lines) is shown, and in the higher strain rate case this is 3.4 times greater than in the slower strain rate case. As previously noted, this is insufficient to compensate for the reduction in time at the higher strain rate ( $\frac{\dot{\epsilon}_{fast}}{\dot{\epsilon}_{slow}} = 8.6$ ).

Figures 7(a) and (b) show the evolution of integrated intensity with time and strain, respectively. This is taken as a proxy for the relative volume fraction of precipitates. These plots show similar behavior to that already discussed for the evolution of Guinier radius, reflecting an accelerating effect of deformation on volume fraction increase, which is greater at the higher strain rate. Close inspection, particularly of Figure 7(b), shows that there is an important difference between the size and volume fraction evolution in the early stages of deformation (strains <3 pct), especially noticeable at the higher strain rate. Unlike the Guinier radius, which increases from the start of the test, the integrated intensity does not initially increase (indeed, it decreases slightly). This suggests that initially the volume fraction does not increase, even though the average precipitate size does. Possible explanations for this behavior are discussed in detail later. The integrated intensity for the non-deformed

case increases only very slightly over the full duration of the test.

Since precipitate size, volume fraction, and number density are all related it is possible to estimate the evolution in relative number density, assuming that the integrated intensity provides a good proxy for the relative precipitate volume fraction. The relative number density evolution calculated in this way is plotted in Figures 7(c) and (d) against time and strain, respectively. These plots show that while the number density for the non-deformed case remains approximately constant, in the deformed case the number density decreases, and this decrease is most rapid after a strain of approximately 5 pct is exceeded (for both strain rates). This suggests that all of the precipitates or clusters that cause the scattering in SAXS are present at the start of the experiment (after quenching and a very short 5 s of hold prior to deformation) and that new nucleation does not lead to a significant increase in the number density of these objects.

#### IV. DISCUSSION

The purpose of this study was to investigate the effect of warm deformation on precipitate evolution in an aluminum alloy starting from an initially supersaturated condition. This can be compared with previous work where the effect of deformation on a pre-existing precipitate distribution formed by pre-aging has been studied.<sup>[2]</sup> One key objective was to determine whether a supersaturated starting condition would lead to a strong effect of deformation on precipitate nucleation under warm deformation conditions.

Considering first the non-deformed material, it was found that clusters were already detected after the quench and initial stabilization hold (5 s at 180 °C) and these clusters evolved only slightly during the subsequent hold (up to 200 s). The measured Guinier radius of approximately 0.56 nm is consistent with the previous studies of cluster size during initial aging of similar alloys<sup>[17]</sup> and corresponds to a cluster containing around 40 to 70 atoms (assuming a 1:1 Zn to Mg ratio<sup>[17]</sup>). The initial clustering process is therefore very rapid, itself probably assisted by the high quenched in vacancy concentration, which at 180 °C is expected to be 10 times higher than the equilibrium concentration.<sup>[17,18]</sup>

These initial clusters were also present in the deformed case before stretching was applied. Therefore, the subsequent evolution of the microstructure appears to be mainly determined by the effect of deformation on these pre-existing clusters rather than a significant effect in leading to nucleation of new clusters. This can be seen from the inferred number density plots, which show that deformation leads to a reduction rather than an increase in number density.

Deformation has been shown to strongly affect the size evolution of the clusters, and this is influenced by both strain and strain rate. The higher strain rate leads to an increase in the mean precipitate growth rate, but this is insufficient to compensate for the shorter time at higher strain rate. Therefore, for a given level of strain,

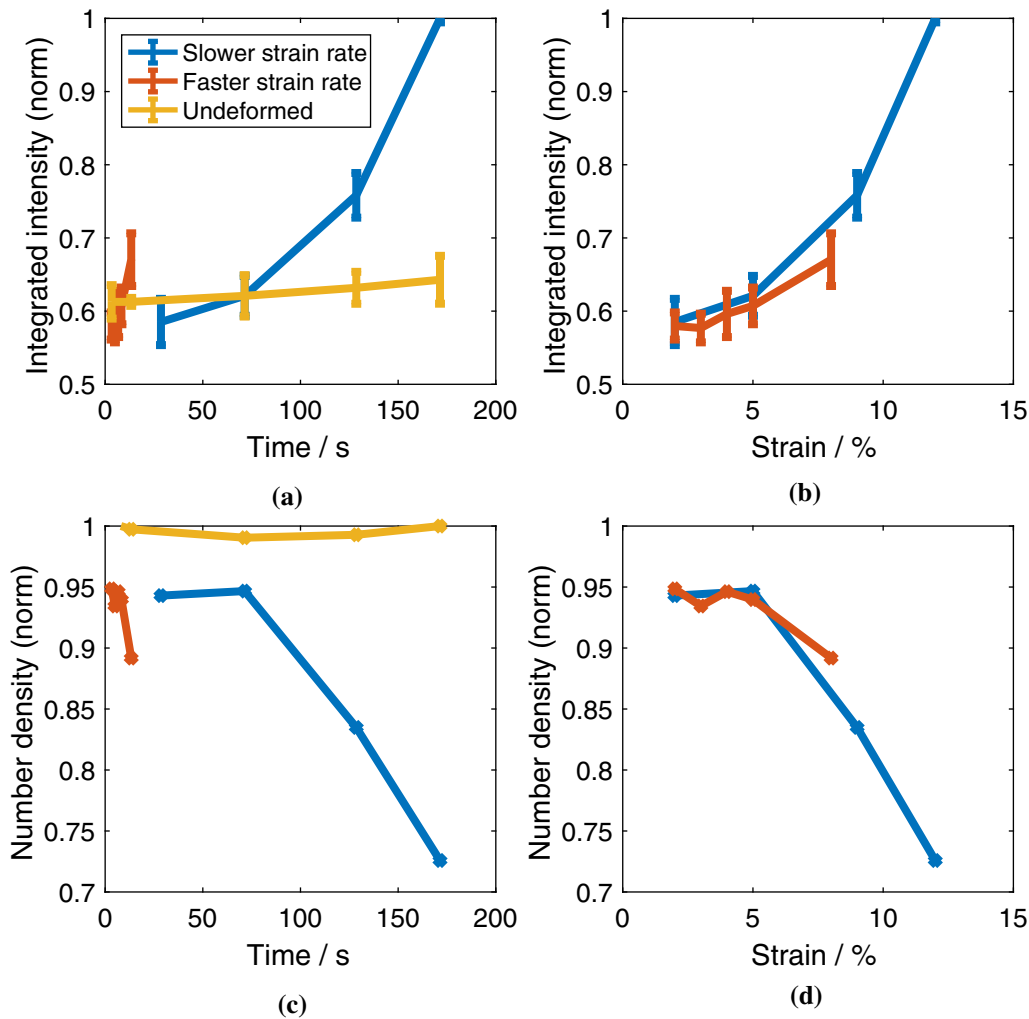


Fig. 7—(a) Evolution of integrated intensity (assumed proportional to volume fraction) for the slower ( $7 \times 10^{-4} \text{ s}^{-1}$ ) and faster ( $6 \times 10^{-3} \text{ s}^{-1}$ ) strain rates compared with the non-deformed case with (a) time, (b) strain. Derived evolution of relative precipitate number density for faster and slower strain rates compared with the non-deformed case plotted as a function of (c) time, (d) strain. Online version in color.

the faster strain rate leads to a slightly smaller average precipitate size than the slower strain rate, and this difference increases with increasing strain. At the early stages of deformation, particularly in the highest strain rate case, the total volume fraction of clusters falls slightly, associated with a reduction in their number density. This may be due to dislocation cutting, causing break up of some of the smaller clusters, with the solute eventually diffusing or being ballistically transported to grow the larger and more stable clusters.

Previous studies have demonstrated that the effect of deformation in similar aluminum alloys can be interpreted mainly by a consideration of the effect of the excess vacancies generated by non-conservative motion of jogs on gliding dislocations. For the temperature and strain rate regimes considered in this study, this effect is expected to be far more significant than direct precipitation on dislocations. TEM provides direct evidence that this is the case since it can be seen that precipitates are quite homogeneously distributed and most are not generally aligned along dislocations or associated

directly with them. In addition, a direct effect of the dislocations should produce a negative strain rate sensitivity,<sup>[1]</sup> which is not observed in this work.

Full details of the excess vacancy effect on deformation enhanced precipitate evolution, and the models to capture this, are considered in detail elsewhere.<sup>[11]</sup> In the present work, a model is used which is based on an adaption of a framework developed by Militzer *et al.* for steels,<sup>[19]</sup> to understand if the excess vacancy effect can explain the observed results.

To summarize this model briefly, it is based on the idea that excess vacancies are created by jogs on gliding dislocations. These excess vacancies can enhance any vacancy mediated process such as substitutional diffusion. Since these vacancies are in excess of the equilibrium thermal vacancy concentration they seek to annihilate, which they will do at sinks such as dislocations and grain boundaries. The total excess vacancy concentration will therefore be controlled by the balance between creation and annihilation mechanisms.



The rate of excess vacancy production can be calculated from this balance. Neglecting the effect of thermal jogs and annihilation of excess vacancies at grain boundaries, which are insignificant for the conditions studied here,<sup>[11]</sup> the excess vacancy production rate is given by

$$\frac{dc_{ex}}{dt} = K_1 \sigma \dot{\epsilon} - K_2 \exp\left(-\frac{Q_m}{kT}\right) \rho_D c_{ex}. \quad [2]$$

The first term is the excess vacancy generation rate, which is simply a proportion of the applied plastic work (determined by the constant  $K_1$ ). The second term is the excess vacancy annihilation rate, which is a function of temperature, the forest dislocation (sink) density  $\rho_D$  and the excess vacancy concentration itself  $c_{ex}$ , scaled by a constant  $K_2$ . Other source and sink terms can be considered,<sup>[19]</sup> but in the case of aluminum under the conditions studied here, they are of low significance. This equation was previously fitted to literature data from *in-situ* studies of precipitate growth evolution during deformation of a similar 7xxx alloy, and the constants  $K_1$  and  $K_2$  relevant to this case were determined.<sup>[11]</sup> A complicating factor is that not only are the excess vacancies evolving during deformation, but so is the sink dislocation density. This is included in the model through a simple and widely used empirical law in which the dislocation density increases from an initial to a saturation value.<sup>[11]</sup>

Figure 8 shows the predictions of this model for (a) lower and (b) higher strain rate studied here. These plots show the total excess vacancies created (the integral of the first term in Eq. [2]), the total excess vacancies annihilated (the integral of the second term in Eq. [2]), and the resultant overall excess vacancy concentration. Also shown is the prediction of the evolving dislocation density. At both strain rates, it can be noted that steady-state has not been reached, either in the evolving

dislocation density or in the excess vacancy concentration. Although this model is not expected to be accurate, the result is consistent with the experimentally measured stress–strain curves which show positive work hardening even at the end of the tests. In addition, the model suggests that at both strain rates, but particularly at the highest strain rate, the annihilation term is much smaller than the creation term across the whole strain range, so that the excess vacancies accumulate with increasing strain.

In both cases, the excess vacancy effect is far from reaching the steady-state that will eventually become established once the creation and annihilation rates reach a point of balance. This is consistent with the previous *in-situ* work on the effect of deformation on the growth of pre-existing precipitates in aluminum alloys, where the results were explained assuming excess vacancy annihilation was negligible.<sup>[2]</sup> Note that this depends strongly on temperature and total applied strain; at higher temperature or higher cumulative strain the annihilation rate increases and eventually a steady-state is established, which is a function of the temperature and strain rate.<sup>[11]</sup>

To explore whether the excess vacancy concentration effect alone could explain the acceleration of growth rate seen with deformation, these two variables were plotted together, as shown in Figure 9 for both lower (a) and higher (b) strain rates. Although the number of experimental data points is limited, it can be seen that in both cases the measured growth rate correlates well with the predicted excess vacancy concentration. At the higher strain rate, the correlation is less good, and there is a misfitting point, but there is significant uncertainty in the measurements. An important point to note is that this good correlation can only be obtained by re-scaling the growth rate axis from the lower to higher strain rate case. This is because application of Eq. [2] predicts that the excess vacancy concentration is relatively insensitive

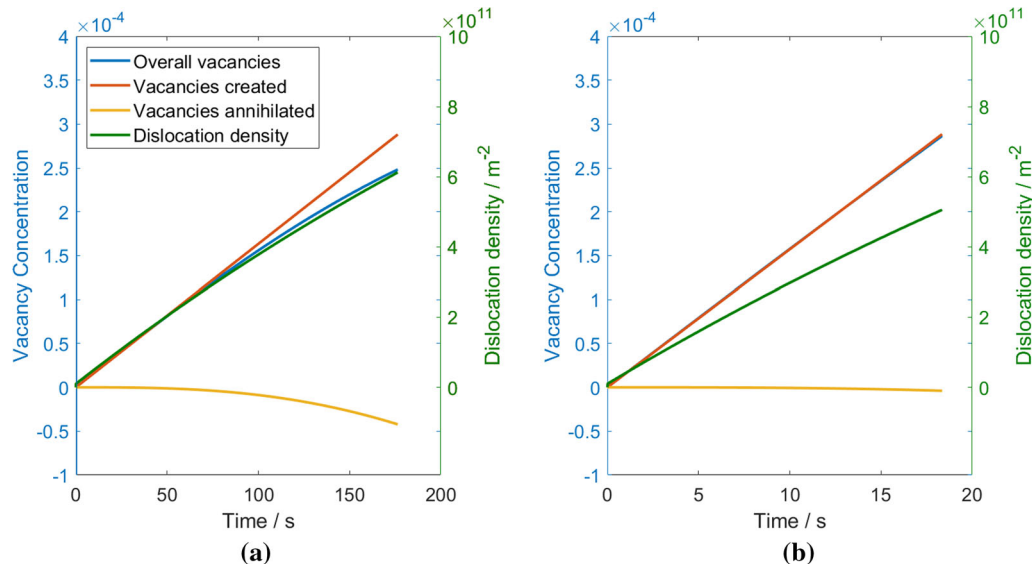


Fig. 8—Calculated evolution of dislocation density and excess vacancy concentration at 180 °C for (a) slower strain rate  $7 \times 10^{-4} \text{ s}^{-1}$ , (b) higher strain rate,  $6 \times 10^{-3} \text{ s}^{-1}$ . Online version in color.

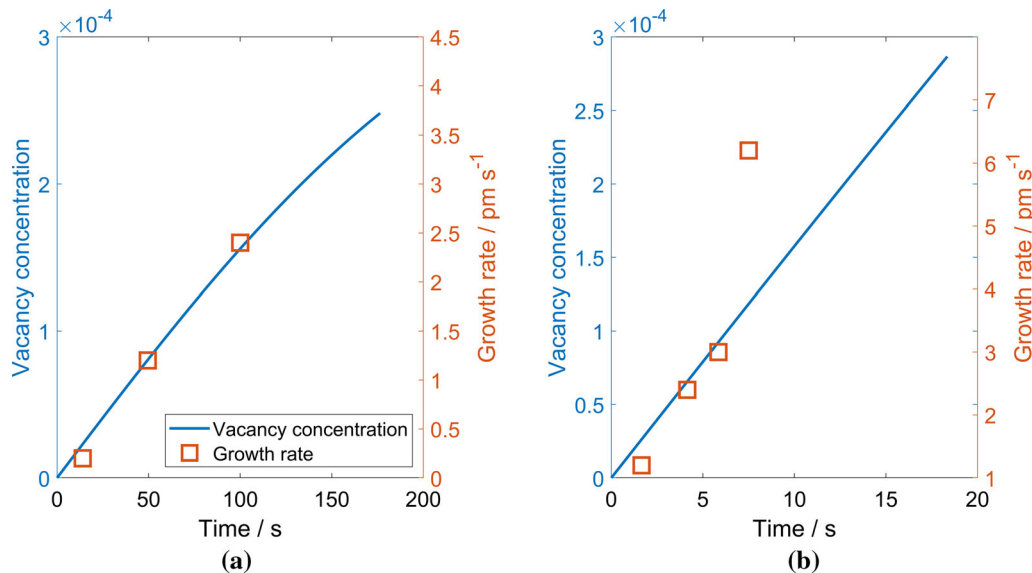


Fig. 9—Measured growth rate and predicted excess vacancy concentration for (a) slower strain rate  $7 \times 10^{-4} \text{ s}^{-1}$ , (b) higher strain rate,  $6 \times 10^{-3} \text{ s}^{-1}$ . Online version in color.

to strain rate in the regime of interest here (where annihilation is almost negligible) and depends only on the accumulated strain. Therefore, the expectation from the model is that the growth rate increase should be approximately independent of the strain rate. However, the experimental results clearly show there is a strain rate effect, with the growth rate increasing 3.4 times more for a given strain increment in the higher strain rate case compared to the lower strain rate case (Figure 6(d)).

The results from this study can be compared with those of Deschamps *et al.*<sup>[2]</sup> who investigated a similar 7xxx alloy but in pre-aged conditions so that there was an initial precipitate population with mean radius of approximately 2 nm. In addition, the range of strain rates used in their study was approximately  $10^{-5}$  to  $10^{-4} \text{ s}^{-1}$  and the deformation/aging temperature was lower at 160 °C. Consistent with the present work, they noted an enhancement in precipitate growth rate due to deformation. Growth rates of 6 to 7 times that in the non-deformed state were observed, which is similar to the growth rate enhancement observed at the higher strain rate and highest strain in the present study. Furthermore, they observed a linear increase in the growth rate with strain, as seen here. No simple monotonic effect of strain rate on the growth enhancement was found in Reference 2 although there was observed to be a factor 3 difference between the greatest and least enhancement at different strain rates, which is similar to the difference obtained here. Deschamps *et al.* also demonstrated that their results were consistent with the excess vacancy effect and that dislocation pipe diffusion can only make a small contribution.<sup>[2]</sup>

The excess vacancy model is therefore successful in explaining much of the behavior observed in the present study and previous work. It correctly predicts the strong enhancement of growth rate with increasing strain, based on the direct relation between excess vacancies

and solute diffusion rates. Even when the initial condition was achieved by rapid quenching from the solutionized state, the initial clustering is so rapid (at least at 180 °C) that in all practical cases the effect of deformation can be understood through its acceleration of growth and coarsening of the initial clusters, rather than an enhancement of nucleation. However, it is also clear that the excess vacancy model ignores some of the complexity of dynamic effects, hidden in the constants  $K_1$  and  $K_2$ , which for quantitative predictions require recalibrating for each temperature and strain rate. These limitations include neglecting the capture of excess vacancies by mobile dislocations, the effect of precipitates on dislocation motion, the dynamic recovery of the forest dislocations into cells, and the heterogeneous distribution of strain. Such effects would likely require a complex dislocation dynamics/precipitate interaction model to capture faithfully.

## V. CONCLUSIONS

This study investigated the effect of deformation on precipitate evolution in AA7075 under warm conditions for the situation where the initial supersaturation of solute is at a maximum in the matrix. To achieve this, experiments were performed in a dilatometer that allowed rapid heating and cooling along with deformation under well controlled conditions. The following conclusions may be drawn from this work:

1. SAXS reveals that small solute clusters are present only 5 s after quenching from solution treatment to the test temperature (180 °C).
2. The evolution of these clusters/precipitates is strongly affected by deformation. This is consistent with an effect on cluster growth rather than nucleation of new clusters or precipitates.

- The precipitates formed during deformation are homogeneously distributed within the matrix. There is no evidence from either TEM or SAXS that deformation enhances the nucleation of new precipitates at the warm stretching temperature used in this study (180 °C).
- Deformation at a faster strain rate leads to a greater average cluster/precipitate growth rate at a given level of strain. However, the acceleration of growth rate with increasing strain rate is not sufficient to compensate for the reduction in time to reach a certain strain level. As a result, for a given strain, the final precipitate size is smaller after deformation at the higher strain rate.
- A simple excess vacancy model can predict the observed linear increase in growth rate with strain. However, the model does not correctly predict the apparent strain rate effect observed in this study, suggesting it is an incomplete description of the complex interactions that occur between deformation and precipitation.

#### ACKNOWLEDGMENTS

Constellium Technology Center is thanked for the provision of materials and financial support for this research. The EPSRC is thanked for financial support through the associated programme grant LightFORM (EP/R001715/1). This work was also supported by the Henry Royce Institute for Advanced Materials, funded through EPSRC grants (EP/R00661X/1, EP/S019367/1, EP/P025021/1, and EP/P025498/1). Dr S. Burholt is thanked for his assistance with the SAXS experiment on the Diamond-Leeds SAXS facility (EP/R042683/1). ZM appreciates the financial support from EPSRC grant Centre for Doctoral Training in Advanced Metallic Systems (EP/S022635/1). JDR acknowledges the support of the DSTL/RAEng Chair in Alloys for Extreme Environments.

#### DATA AVAILABILITY

The data required to reproduce these findings are available from the LightFORM Zenodo repository <https://zenodo.org/communities/lightform/>.

#### CONFLICT OF INTEREST

On behalf of all authors, the corresponding author states that there is no conflict of interest.

#### OPEN ACCESS

This article is licensed under a Creative Commons Attribution 4.0 International License, which permits use, sharing, adaptation, distribution and reproduction in any medium or format, as long as you give appropriate credit to the original author(s) and the source, provide a link to the Creative Commons licence, and indicate if changes were made. The images or other third party material in this article are included in the article's Creative Commons licence, unless indicated otherwise in a credit line to the material. If material is not included in the article's Creative Commons licence and your intended use is not permitted by statutory regulation or exceeds the permitted use, you will need to obtain permission directly from the copyright holder. To view a copy of this licence, visit <http://creativecommons.org/licenses/by/4.0/>.

#### REFERENCES

- A. Deschamps, F. Bley, F. Livet, D. Fabregue, and L. David: *Philos. Mag.*, 2003, vol. 83, pp. 677–92.
- A. Deschamps, G. Fribourg, Y. Bréchet, J.L. Chemin, and C.R. Hutchinson: *Acta Mater.*, 2012, vol. 60, pp. 1905–16.
- C.R. Hutchinson, F. De Geuser, Y. Chen, and A. Deschamps: *Acta Mater.*, 2014, vol. 74, pp. 96–109.
- W. Mirihanage, J.D. Robson, S. Mishra, P. Hidalgo-Manrique, J.Q. Da Fonseca, C. Daniel, P. Prangnell, S. Michalik, O. Magdysyuk, and T. Connolly: *Acta Mater.*, 2021, vol. 205, p. 116532.
- M.J. Starink, N. Gao, N. Kamp, S.C. Wang, P.D. Pitcher, and I. Sinclair: *Mater. Sci. Eng. A*, 2006, vol. 418, pp. 241–49.
- W. Sun, Y. Zhu, R. Marceau, L. Wang, Q. Zhang, X. Gao, and C. Hutchinson: *Science*, 2019, vol. 363, pp. 972–75.
- Y. Zhang, S. Jin, P.W. Trimby, X. Liao, M.Y. Murashkin, R.Z. Valiev, J. Liu, J.M. Cairney, S.P. Ringer, and G. Sha: *Acta Mater.*, 2019, vol. 162, pp. 19–32.
- L. Couturier, A. Deschamps, F. De Geuser, F. Fazeli, and W.J. Poole: *Scr. Mater.*, 2017, vol. 136, pp. 120–23.
- G. Saada: *Physica*, 1961, vol. 27, pp. 657–60.
- G. Saada: *Acta Metall.*, 1961, vol. 9, pp. 166–68.
- J.D. Robson: *Metall. Mater. Trans. A*, 2020, vol. 51, pp. 5401–13.
- w? > F. De Geuser and A. Deschamps: *C. R. Phys.*, 2012, vol. 13, pp. 246–56.
- G. Sha and A. Cerezo: *Surf. Interface Anal.*, 2004, vol. 36, pp. 564–68.
- A. Deschamps, and F. De Geuser: *J. Appl. Crystallogr.*, 2011, vol. 44, pp. 343–52.
- A. Deschamps and F. De Geuser: *Metall. Mater. Trans. A*, 2013, vol. 44, pp. 77–86.
- L. Ding, L. Zhao, Y. Weng, D. Schryvers, Q. Liu, and H. Idrissi: *J. Alloys Compd.*, 2021, vol. 851, p. 156890.
- P. Schloth, J. Wagner, J. Fife, A. Menzel, J.-M. Drezet, and H. Van Swygenhoven: *Appl. Phys. Lett.*, 2014, vol. 105, p. 101908.
- P. Schloth, A. Deschamps, C.-A. Gandin, and J.-M. Drezet: *Mater. Des.*, 2016, vol. 112, pp. 46–57.
- M. Militzer, W. Sun, and J. Jonas: *Acta Metall. Mater.*, 1994, vol. 42, pp. 133–41.

**Publisher's Note** Springer Nature remains neutral with regard to jurisdictional claims in published maps and institutional affiliations.